Computers and Structures 87 (2009) 812–827

Contents lists available at ScienceDirect

Computers and Structures

journal homepage: www.elsevier.com/locate/compstruc

High-order accurate simulation of low-Mach laminar flow past two side-by-side cylinders using spectral difference method

Chunlei Liang *, Sachin Premasuthan, Antony Jameson

Aeronautics and Astronautics, Stanford University, Durand 005, Stanford, CA 94305, United States

ARTICLE INFO

Article history:
Received 10 December 2008
Accepted 22 December 2008
Available online 27 February 2009

Keywords:
Spectral difference method
Curved wall boundary
Unstructured grid

ABSTRACT

This paper reports development of a two-dimensional solver for compressible viscous flow using spectral difference (SD) method and its applications on simulating laminar flow past two side-by-side cylinders at various spacings. The high-order spectral difference solver is based on unstructured quadrilateral grids. High-order curved wall boundary representation is developed for cylinders. Nine different spacings (center-to-center distance/diameter s = 1.1, 1.4, 1.5, 1.7, 2, 2.5, 3, 3.4 and 4) are investigated. The simulation results are compared to experimental results and other numerical results. As s increases, single bluff-body, flip-flopping, anti-symmetric and symmetric wake patterns are predicted.

Published by Elsevier Ltd.

1. Introduction

1.1. Flow past two side-by-side cylinders

Investigations of the fluid flow and vortex dynamics about simple configurations of two cylinders help our understanding of the flows around more complex and larger-scale structures, for instance the flow around tube banks employed in process industries [14] and especially in the power generation and oil industry as well as flow around neighboring buildings and river flow vegetation, etc. Other applications are also related to two cylinders such as hollow fiber arrays with many applications in absorption, extraction and ultra-filtration [12] or paper machine forming fabrics [9]. In the latter examples, the flows are laminar with Reynolds number in the range of 150–200.

Zdravkovich [34,35] has reviewed the problem of mutual interference between pairs of cylinders in a steady flow. Much attention was paid to the side-by-side and inline arrangements of the cylinder pair. Williamson [31] suggested that a spacing between two side-by-side cylinders with the ratio of distance between cylinder centers to the diameter (s) in the range of 2–6 produces vortex-shedding synchronization. The resulting wake configuration will be either two parallel streets in antiphase mode or a binary-vortex street mode which consists of a street being composed of pairs of like-signed vortices rotating around one another with Reynolds number in the range of 100–200. Experimental results were also obtained by Zhou et al. [36] at relatively low Reynolds numbers (150–450). They suggested that the flow pattern is very much independent of Reynolds number of this range. At s = 3, they observed the anti-phase flow patterns for all Reynolds numbers using more advanced flow visualization methods. Chang and Song [3] made an early investigation of laminar flow past two side-by-side cylinders using a blending technique of finite-element method and finite-difference method. Recently, numerical simulations have been performed for incompressible laminar flow past two side-by-side cylinders by various methods. For instance, Meneghini et al. [18] used a finite-element unstructured method, Kang [10] and Lee et al. [11] employed a finite-volume structured method with immersed boundary technique and Ding et al. [7] developed a mesh-free finite-difference method and studied this particular configuration.

The above studies mentioned are all about incompressible flows. The simulation codes commonly attained at best second-order accuracy in space. Furthermore, all the above discussed numerical simulations employed only piecewise linear wall boundary conditions or some kind of interpolation schemes to satisfy no-slip condition for immersed boundary method. The present simulation uses a recently developed Spectral Difference high-order unstructured method to simulate a low-Mach number compressible laminar flow past two side-by-side cylinders. A cubic spline curve fitting routine is programmed into our solver and it allows an automatic construction of a cubic curved wall boundary condition for each cylinder.

1.2. Spectral difference method

Until recently, compressible flow computations on unstructured meshes have generally been dominated by schemes restricted to second order accuracy. However, the need for highly

* Corresponding author. Tel.: +1 650 724 5479.
E-mail address: chliang@stanford.edu (C. Liang).

0045-7949/$ - see front matter Published by Elsevier Ltd.
doi:10.1016/j.compstruc.2008.12.016

accurate methods in applications such as large eddy simulation, direct numerical simulation, computational aero-acoustics etc., has seen the development of higher order schemes for unstructured meshes such as the discontinuous Galerkin (DG) method [4,5,1], spectral volume (SV) method [29,17,30] and spectral difference (SD) method [16,28,13]. The SD method is a newly developed efficient high-order approach based on differential form of the governing equation. It was originally proposed by Liu et al. [16] and developed for wave equations in their paper on triangular grids. Wang et al. [28] extended it to 2D Euler equations on triangular grids and Liang et al. [13] improved the convergence of the method using implicit LU-SGS and p-multigrid schemes. Recently, Sun et al. [27] further developed it for three-dimensional Navier–Stokes equations on hexahedral unstructured meshes. Mohammad et al. [21] investigated flow past a circular cylinder at subcritical Reynolds number using the SD method. The SD method combines elements from finite-volume and finite-difference techniques. Similar to the discontinuous Galerkin (DG) and spectral volume (SV) methods, the SD scheme achieves high-order accuracy by locally approximating the solutions as a high degree polynomial inside each cell. However, being based on the differential form of the equations, its formulation is simpler than that of the DG and SV methods as no test function or surface integral is involved. Conservation properties are still maintained by a judicious placement of the nodes at quadrature points of the chosen simplex.

This paper presents development of a new in-house two-dimensional high-order SD code for viscous compressible flow. The formulations are similar to the ones used by Sun et al. [27]. Previous numerical studies on two side-by-side cylinders have not concluded the effect of tube spacings on flow separation points, wake flow pattern and force coefficients. The SD method is employed in this paper to study the unsteady laminar flow past a pair of side-by-side cylinders with nine different spacings (center-to-center distance/diameter s = 1.1, 1.4, 1.5, 1.7, 2, 2.5, 3, 3.4 and 4). We aim to see the effect of the spacings on flow pattern, separation points and flow exerted forces.

The paper is organized as follows. Section 2 describes the numerical approach and solution methods. In order to validate the spatial accuracy of the code, Section 3 presents two cases with analytical solutions and simulation results obtained by the SD method in addition to a simulation of flow past an isolated cylinder with detailed comparisons to other results. Section 4 reports the simulation results obtained for laminar viscous flows past two side-by-side cylinders. Finally, Section 5 summarizes the main findings of this work.

2. Numerical formulation

The formulation of the equations is similar to the formulation of Sun et al. [27] for unstructured hexahedral grids.

Consider the unsteady compressible 2D Navier–Stokes equations in conservative form

$$\frac{\partial Q}{\partial t}+\frac{\partial F}{\partial x}+\frac{\partial G}{\partial y}=0 \tag{1}$$

where Q is the vector of conserved variables; F and G are the total fluxes including both inviscid and viscous flux vectors. To achieve an efficient implementation, all elements in the physical domain (x,y) are transformed into a standard square element $(0\leqslant\xi\leqslant 1, 0\leqslant\eta\leqslant 1)$ as shown in Fig. 1. The transformation can be written as

$$\begin{pmatrix}x\\ y\end{pmatrix}=\sum_{i=1}^{K}M_i(\xi,\eta)\begin{pmatrix}x_i\\ y_i\end{pmatrix} \tag{2}$$

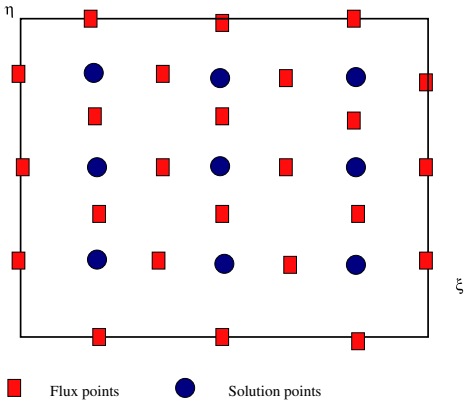

Fig. 1. Distribution of flux and solution points for the third order SD scheme.

where K is the total number of points used to define the physical element, (x_i,y_i) are the cartesian coordinates of those points, and $M_i(\xi,\eta)$ are the shape functions. For elements with straight edges, K is equal to 4. For elements lying on curved boundaries, 8 points (four mid-edge and four corner points) can define a quadratic representation and 12 points can determine a third-order cubic representation. The metrics and the Jacobian of the transformation can be computed for each element. The Jacobian can be expressed as follows:

$$J=\begin{pmatrix}x_\xi & x_\eta\\ y_\xi & y_\eta\end{pmatrix} \tag{3}$$

The governing equations in the physical domain are then transferred into the computational domain, and the transformed equations take the following form:

$$\frac{\partial\tilde{Q}}{\partial t}+\frac{\partial\tilde{F}}{\partial\xi}+\frac{\partial\tilde{G}}{\partial\eta}=0 \tag{4}$$

where $\tilde{Q}=|J|\cdot Q$ and

$$\begin{pmatrix}\tilde{F}\\ \tilde{G}\end{pmatrix}=|J|J^{-1}\begin{pmatrix}F\\ G\end{pmatrix} \tag{5}$$

In the standard element, two sets of points are defined, namely the solution points and the flux points as illustrated in Fig. 1.

In order to construct a degree $(N-1)$ polynomial in each coordinate direction, solutions at N points are required. The solution points in 1D are chosen to be the Gauss points defined by

$$X_s=\frac{1}{2}\left[1-\cos\left(\frac{2s-1}{2N}\cdot\pi\right)\right],\quad s=1,2,\ldots,N \tag{6}$$

The flux points are selected to be the Gauss–Lobatto points given by

$$X_{s+1/2}=\frac{1}{2}\left[1-\cos\left(\frac{s}{N}\cdot\pi\right)\right],\quad s=0,1,\ldots,N \tag{7}$$

Using the solutions at N solution points, a degree $(N-1)$ polynomial can be built using the following Lagrange basis:

$$h_i(X)=\prod_{s=0,s\neq i}^{N}\left(\frac{X-X_s}{X_i-X_s}\right) \tag{8}$$

Similarly, using the fluxes at $(N+1)$ flux points, a degree N polynomial can be built for the flux using a similar Lagrange basis

$$l_{i+1/2}(X)=\prod_{s=0,s\neq i}^{N}\left(\frac{X-X_{s+1/2}}{X_{i+1/2}-X_{s+1/2}}\right) \tag{9}$$

The reconstructed solution for the conserved variables in the standard element is just the tensor products of the two one-dimensional polynomials,

$$\tilde{Q}(\xi,\eta)=\sum_{j=1}^{N}\sum_{i=1}^{N}\tilde{Q}_{ij}h_i(\xi)\cdot h_j(\eta) \tag{10}$$

Similarly, the reconstructed flux polynomials take the following form:

$$\begin{aligned}\tilde{F}(\xi,\eta)&=\sum_{j=1}^{N}\sum_{i=0}^{N}\tilde{F}_{i+1/2,j}l_{i+1/2}(\xi)\cdot h_j(\eta),\\ \tilde{G}(\xi,\eta)&=\sum_{j=0}^{N}\sum_{i=1}^{N}\tilde{G}_{ij+1/2}h_i(\xi)\cdot l_{j+1/2}(\eta)\end{aligned} \tag{11}$$

The reconstructed fluxes are only element-wise continuous, but discontinuous across cell interfaces. For the inviscid flux, a Riemann solver is employed to compute a common flux at interfaces to ensure conservation and stability. In our case, we have used the Riemann problem solver (Rusanov [24] or Roe [23] with entropy fixing approach like Harten and Hyman [8]) to compute the interface fluxes.

In summary, the algorithm to compute the inviscid flux derivatives consists of the following steps:

(1) Given the conservative variables at the solution points, the conservative variables are computed at the flux points
(2) The inviscid fluxes at the interior flux points are computed using the solutions computed at Step (1)
(3) The inviscid fluxes at the element interfaces are computed using the Rusanov/Roe solver. Given the normal direction of the interface n, and the averaged normal velocity component V_n and the sound speed c, the inviscid flux on the interface can be determined.
(4) The derivatives of the fluxes are computed at the solution points using the derivatives of Lagrange operators l

$$\begin{aligned}\left(\frac{\partial\tilde{F}}{\partial\xi}\right)_{i,j}&=\sum_{r=0}^{N}\tilde{F}_{r+1/2,j}\cdot l'_{r+1/2}(\xi_i),\\ \left(\frac{\partial\tilde{G}}{\partial\eta}\right)_{i,j}&=\sum_{r=0}^{N}\tilde{G}_{i,r+1/2}\cdot l'_{r+1/2}(\eta_j)\end{aligned} \tag{12}$$

We write inviscid and viscous fluxes separately for Eq. (1) as

$$\frac{\partial Q}{\partial t}+\nabla F_e(Q)-\nabla F_v(Q,\nabla Q)=0 \tag{13}$$

where the conservative variables Q and Cartesian components $f_e(Q)$ and $g_e(Q)$ of the inviscid flux vector $F_e(Q)$ are given by

$$Q=\begin{Bmatrix}\rho\\ \rho u\\ \rho v\\ E\end{Bmatrix},\quad f_e(Q)=\begin{Bmatrix}\rho u\\ \rho u^2+p\\ \rho uv\\ u(E+p)\end{Bmatrix},\quad g_e(Q)=\begin{Bmatrix}\rho v\\ \rho uv\\ \rho v^2+p\\ v(E+p)\end{Bmatrix} \tag{14}$$

Here ρ is the density, u and v are the velocity components in x and y directions, p stands for pressure and E is the total energy. The pressure is related to the total energy by

$$E=\frac{p}{\gamma-1}+\frac{1}{2}\rho(u^2+v^2) \tag{15}$$

with a constant ratio of specific heat γ. For all test cases in the present study, γ is going to be 1.4 for air.

The Cartesian components $f_v(Q,\nabla Q)$ and $g_v(Q,\nabla Q)$ of viscous flux vector $F_v(Q,\nabla Q)$ are given by

$$\begin{aligned}f_v(Q,\nabla Q)&=\mu\begin{Bmatrix}0\\ 2u_x+\lambda(u_x+v_y)\\ v_x+u_y\\ u[2u_x+\lambda(u_x+v_y)]+v(v_x+u_y)+\frac{C_p}{P_r}T_x\end{Bmatrix},\\ g_v(Q,\nabla Q)&=\mu\begin{Bmatrix}0\\ v_x+u_y\\ 2v_y+\lambda(u_x+v_y)\\ v[2v_y+\lambda(u_x+v_y)]+u(v_x+u_y)+\frac{C_p}{P_r}T_y\end{Bmatrix}\end{aligned} \tag{16}$$

where μ is the dynamic viscosity, C_p is the specific heat and P_r stands for Prandtl number. T is temperature which can be derived from the perfect gas assumption. λ is set to $-2/3$ according to the Stokes hypothesis.

The solution procedures to get viscous fluxes can be described as the following steps.

- Reconstruct Q_f at the flux points from the conservative variables at the solution points using Eq. (10).
- Average the field of Q_f on the element interfaces as $\overline{Q_f}=\frac{1}{2}(Q_f^L+Q_f^R)$. For interior flux points, $\overline{Q_f}=Q_f$. Meanwhile, appropriate boundary conditions shall be applied for specific edge flux points.
- Evaluate ∇Q from $\overline{Q_f}$ using Eq. (12) where $\nabla Q=\begin{Bmatrix}Q_x\\ Q_y\end{Bmatrix}$ and $Q_x=\frac{\partial Q}{\partial\xi}\xi_x+\frac{\partial Q}{\partial\eta}\eta_x$, etc.

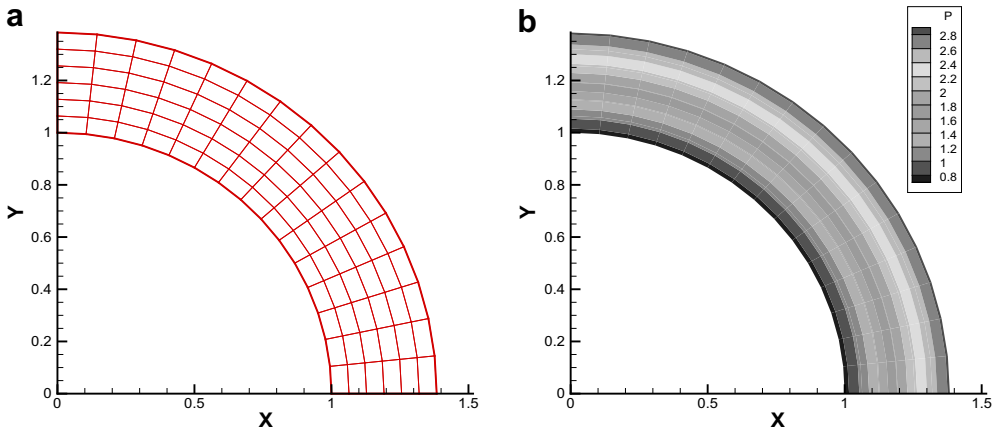

Fig. 2. Supersonic vortex flow obtained using grid of 6×15.

Table 1
L^2 errors and orders of accuracy of inviscid supersonic vortex flow.

No. of elements	No. of DOFs	L2-error	Order
2nd order SD			
40	160	4.7249E−03	–
90	360	1.9881E−03	2.135
360	1440	4.4721E−04	2.152
1440	5760	1.0196E−04	2.133
3rd order SD			
40	360	3.3393E−04	–
90	810	9.8833E−05	3.003
360	3240	1.2242E−05	3.013
1440	12960	1.5230E−06	3.007
4th order SD			
40	640	1.9238E−05	–
90	1440	3.7883E−06	4.008
360	5760	2.3651E−07	4.002
1440	23040	1.4743E−08	4.004

- Reconstruct ∇Q, from Eq. (10) and applying appropriate boundary conditions for specific flux points and average them on the element interfaces as $\overline{\nabla Q_f} = \frac{1}{2}(\nabla Q_f^L + \nabla Q_f^R)$.
- Use $\overline{Q_f}$ and $\overline{\nabla Q_f}$ in order to compute viscous flux vectors described in Eq. (16) at the element interfaces.

Flows with either steady or unsteady solutions are considered in this paper. In order to solve the flow to a steady state from a nearly arbitrary initial guess, a relaxation scheme is needed. Therefore, the time derivative term is retained for both steady and unsteady cases.

All computations in this paper are advanced in time using a fourth-order strong-stability-preserving five-stage Runge–Kutta scheme. It is written in the form of Eq. (17).

$$\begin{aligned} Q^{(0)} &= Q^n; \\ Q^{(i)} &= \sum_{k=0}^{i-1}[\alpha_{i,k}Q^k + \Delta t\beta_{i,k}R(Q^k)], \quad i = 1,2,\ldots,s; \\ Q^{(n+1)} &= Q^s \end{aligned} \tag{17}$$

where $s = 5$ for a five stage Runge–Kutta scheme. The coefficients α_{ik} and β_{ik} are taken from the table of SSPRK(5,4) in Spiteri and Ruuth [26]. The suitability of this Runge–Kutta scheme for future study of unsteady turbulent flow using LES or DNS is not investigated here as this paper focuses on low Reynolds number laminar flow. Interested readers can refer to Debonis and Scott [6] and Ragab and El-Okda [22] for their Large Eddy Simulation investigations with an explicit five-stage fourth-order Runge–Kutta scheme.

3. Accuracy validation

In the following, an inviscid flow case with analytical solution is chosen to demonstrate the order of accuracy. An inviscid flow past a circle case is used to illustrate the effects of grid-refinement and increment of polynomial order. A viscous flow case with analytical solution is also selected in order to demonstrate the order of accu-

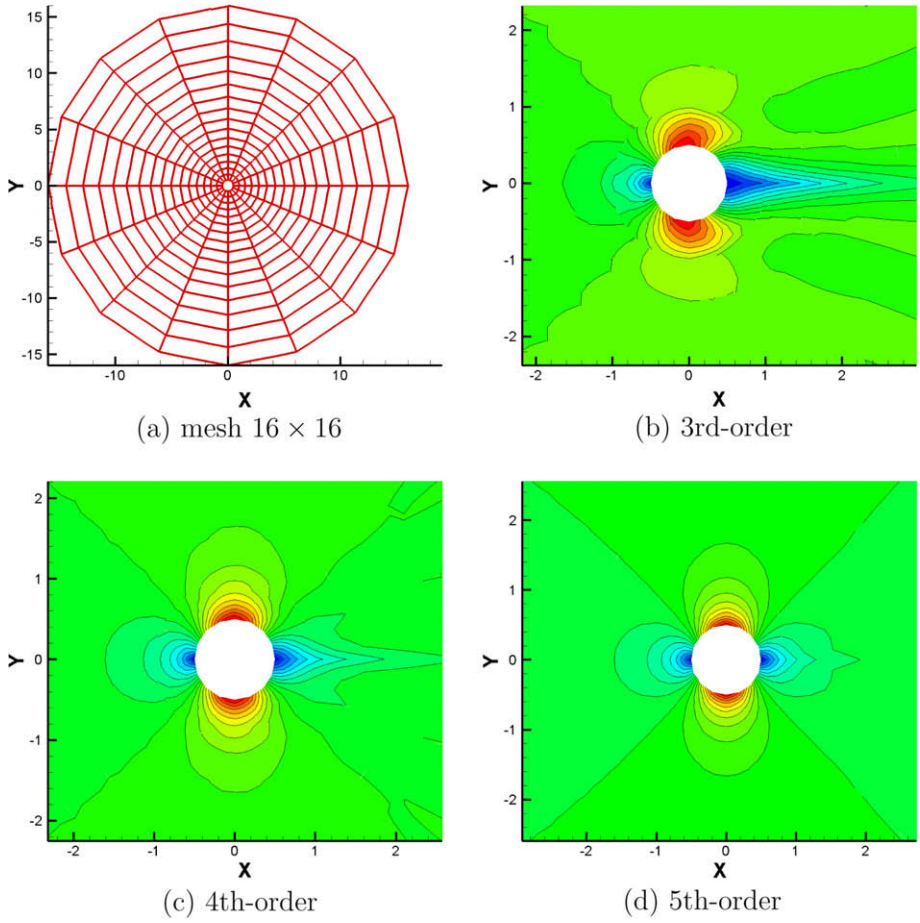

Fig. 3. Mach contour obtained by different order SD methods on cubic wall boundaries using grid 16 × 16.

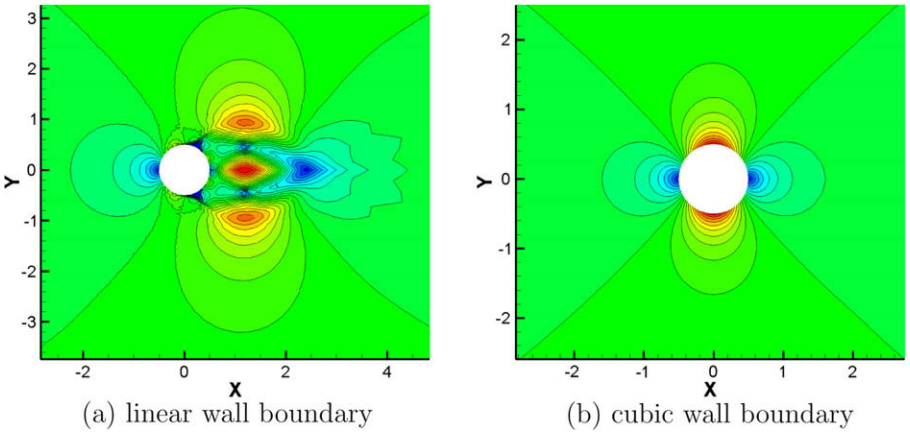

Fig. 4. Mach number contour predicted by the 4th order SD with linear or cubic wall boundaries using grid 32×32.

racy of the implemented SD method for both inviscid and viscous fluxes. It is followed by the classical test case of laminar flow past an isolated cylinder at Re = 100.

3.1. Validation using supersonic vortex flow

The supersonic vortex flow problem is one of the few non-trivial problems of the compressible 2D Euler equations for which a smooth analytical solution is known. The inviscid, isentropic, supersonic flow of a compressible fluid between concentric circular arcs presents a flow where the velocity varies inversely with radius. The expression for density as a function of radius r is given by

$$\rho(r) = \rho_i \left\{ 1 + \frac{\gamma - 1}{2} M_i^2 \left[1 - \left(\frac{r_i}{r} \right)^2 \right] \right\}^{\frac{1}{\gamma - 1}} \tag{18}$$

where M_i and r_i are the Mach number and the radius at the inner arc. In the present calculation, the Mach number, density and pressure at the inner radius r_i are specified to be 2.25, 1 and $1/\gamma$ respectively. The inner and outer radii are 1 and 1.384. The outer arc and bottom boundaries are fixed with analytical solutions. The zero-gradient extrapolation boundary is employed for the exit. In the following, the numerical solution to this problem are computed for the 2nd, 3rd and 4th order SD method on successively refined grids. All the computations are initialized using constant density and pressure. The $L2$ error of the density is evaluated.

The four meshes used in the computation were of sizes 10×4, 15×6, 30×12, and 60×24. A sample 15×6 mesh is shown in Fig. 2a. Fig. 2b shows the pressure contours in the flow field obtained by the 3rd order SD method. The details of the order calculation and verification are shown in Table 1. The results obtained in the table clearly indicate that the SD method applied to the steady compressible Euler equations exhibits a full order of convergence on smooth solutions. It provides the details of the spatial accuracy of the SD method for different orders for this numerical experiment. One can also see the $L2$-error of the SD method at different order against the number of degrees of freedom. One can also clearly see that a higher order SD method requires a less number of degrees of freedom than a lower order SD method in order to achieve the same accuracy.

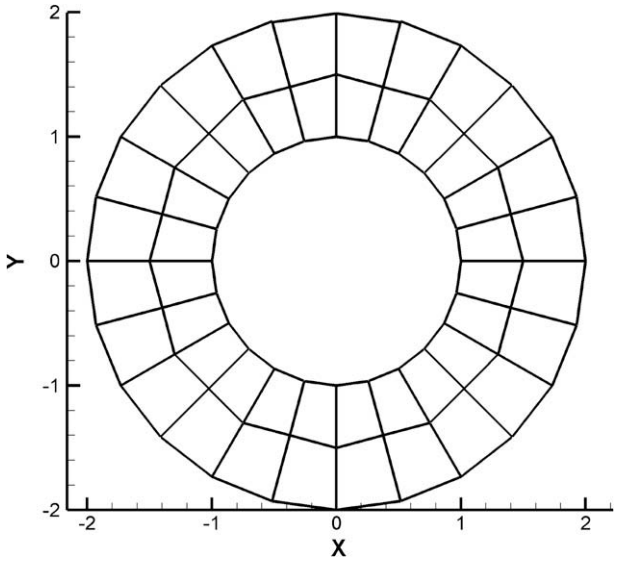

Fig. 5. Grid 24×2 for Taylor-Couette Flow.

3.2. Inviscid flow past a circle

Fig. 3a shows a grid with only 16 cells around the periphery of a circle. The inviscid Euler equations are solved using the SD method. The Dirichlet boundary condition is used for the outer circle. For the near wall cells, we can have both 8-point quadratic representation and 12-point cubic representation as aforementioned. Varying the polynomial order N and using the cubic representation for the wall boundary, we can show that the predicted results are improving gradually on the mesh with 16×16 cells as the order increases. Fig. 3b–d show the Mach number contour obtained by the 3rd-order, 4th-order and fifth-order SD methods respectively.

For high-order numerical schemes, inviscid flow past a circle requires a good curved wall representation for high-order schemes as already discussed by Bassi and Rebay [1]. In order to demon-

Table 2
L^2 errors and orders of accuracy of viscous Taylor-Couette flow.

No. of elements	No. of DOFs	L2-error	Order
3rd order SD			
48	432	8.896e-4	–
192	1728	1.002e-4	3.15
768	6912	1.084e-5	3.21
4th order SD			
48	768	1.482e-4	–
192	3072	1.004e-5	3.88
768	12288	6.575e-7	3.93

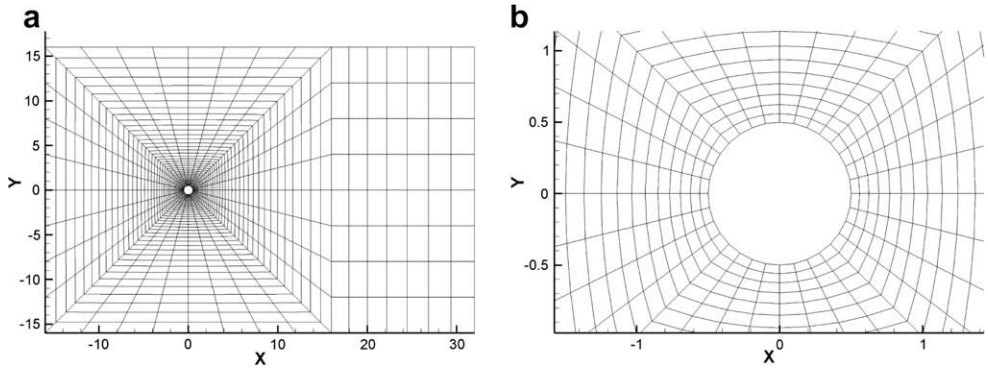

Fig. 6. Computational grid for unsteady flow past a cylinder.

strate its effect, we use another computational grid with 32×32 cells. As shown in Fig. 4a, the linear wall representation deteriorates the results predicted by the 4th-order SD method on the finer mesh. The results are even less accurate than the ones obtained by the 3th-order SD method on a computational grid with 16×16 with a cubic wall boundary shown in Fig. 3b. Nevertheless, the symmetrical Mach number contour is predicted correctly by the 4th-order SD method when a cubic wall representation is used as shown in Fig. 4b.

3.3. Validation using compressible Taylor-Couette flow

The numerical order of accuracy is validated using compressible Taylor-Couette flow with analytical solution. This test problem was taken from a recent paper presented by Michalak and Ollivier-Gooch [19]. The Reynolds number is 10 based on inner cylinder spinning tangential velocity and its radius (=1). The temperature and pressure are prescribed for the inner cylinder which determine a Mach number equal to 0.5. An adiabatic wall boundary condition is employed for the stationary outer cylinder. A grid with 24×2 cells is shown in Fig. 5. Two other finer grids are obtained using successive grid refinements in both directions. A cubic curved wall boundary is programmed for both inner and outer cylinders. We obtained desired numerical order $L2$ accuracy as shown in Table 2. The maximum accuracy of fourth-order is demonstrated for y velocity in the table. The explicit Runge–Kutta scheme becomes slow when the polynomial order is increased. However, the fifth-order and even higher accuracy can also be demonstrated using the implicit LU-SGS method and p-multigrid approach with a significantly shorter CPU time [13].

Table 3
Comparison of present results against other results for flow over a cylinder at Reynolds number 100.

Investigator	Present	Sharman 05	Mene-01	Kang [10]	Ding 07
Re no.	100	100	100	100	100
Nodes	33400	14,441	13,696	62,127	23,033
Blockage	0.0312	0.02	0.047	–	–
C_l'	0.232	0.23	–	0.32	0.287
$\overline{C_d}$	1.365	1.33	1.37	1.33	1.356
C_d'	0.0086	0.0064	–	–	0.01
St. no.	0.164	0.164	0.165	0.165	0.166

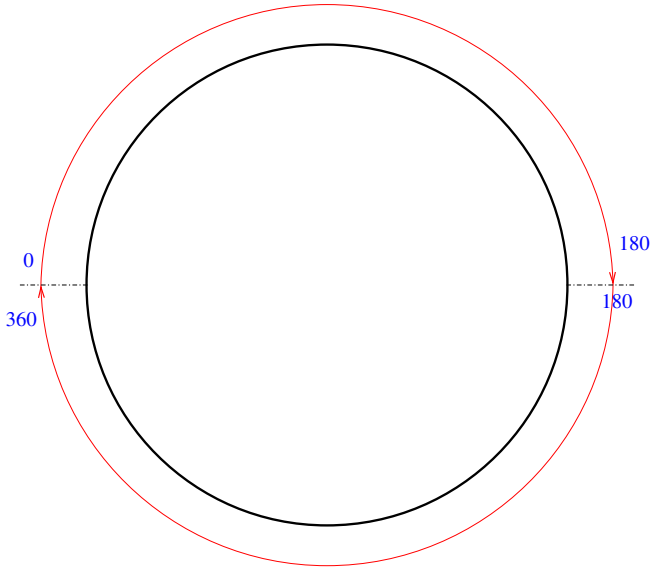

Fig. 8. Degree definition of a cylinder for skin friction coefficient.

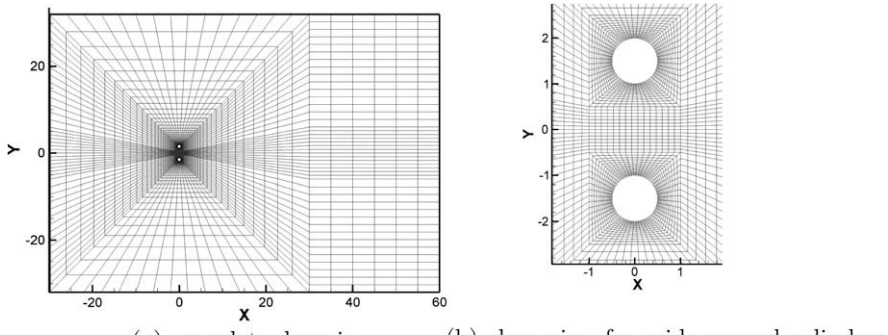

Fig. 7. Computational grid for flow past two side-by-side cylinders at $s = 3$.

Having validated the order of spatial accuracy using test problems with steady flow solutions, we will look at the simulation of the unsteady flow past an isolated cylinder at Re = 100 with comparison between our results and other published results.

3.4. Viscous flow past one cylinder

Fig. 6 shows the computational grid for the unsteady flow past a single cylinder. There are 32 cells around the circumference of the cylinder. The first cell next to the cylinder wall has a spacing around 11% cylinder radius in the normal direction. The level of grid resolution is much coarser than the one used in Maeneghini et al. [18] who employed 128 points around the cylinder wall and the first node had a distance about 1% of cylinder radius for an isolated cylinder case. The computation for this case is performed using the fifth-order SD method and a cubic curved wall boundary condition is employed for the cylinder surface. Dirichlet boundary condition is used for the inlet and fixed-pressure is adopted for the outlet boundary condition. Inviscid symmetry boundary conditions are applied on the two lateral sides. The initial condition is provided according to the free-stream condition as $u = u_\infty, v = 0, p = p_\infty$ and $\rho = \rho_\infty$.

The SD method offers a flexibility in adjusting the number of degrees of freedom for different grid resolution. We only need to vary one parameter in our solver for the polynomial degree N. The difference of the fluctuating lift coefficient C_l' predicted by the 4th-order (total DOFs 21,376) and the fifth-order SD methods (total DOFs 33,400) and the difference of coefficient C_d' are all less than 2%. In the following for an isolated cylinder case, we only present the results obtained by the fifth-order SD method.

Table 3 reports the comparison between present computation of compressible viscous flow at Mach number 0.2 to other numerical and experimental studies for incompressible viscous flow at the same Reynolds number 100. The Strouhal number predicted by the SD method on a mesh with degree-of-freedom 33,400 is identical to the one predicted by Sharman et al. [25] and the measured value by Williamson [32]. There is a separate compressible flow simulation which is not included in the table. Mittal and Tezduyar [20] also predicted 0.164 using a finite-element compressible flow solver at Re = 100 and Mach number 0.2. The SD method predicted C_l' is identical to the one predicted by the

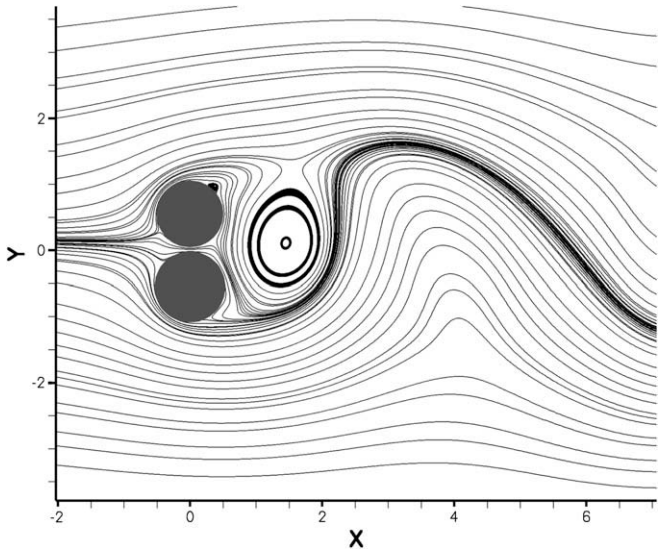

Fig. 9. Streamlines for $s = 1.1$ and Re = 100.

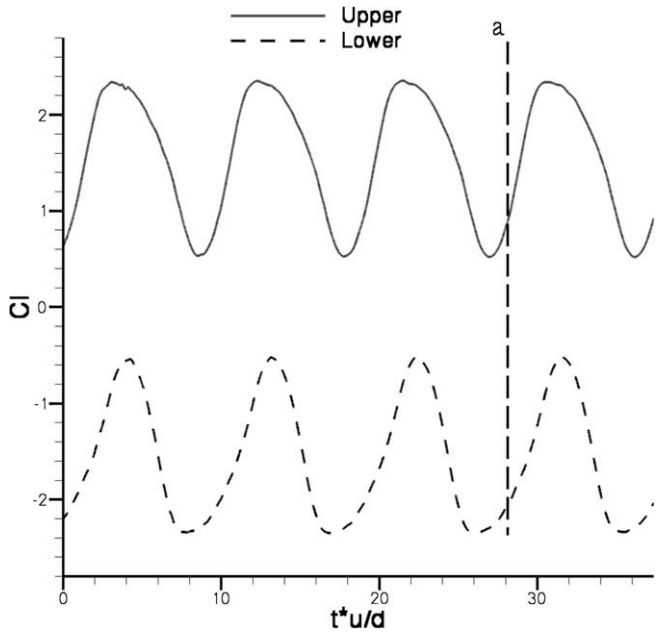

Fig. 10. Time history of lift coefficients for Re = 100 and $s = 1.1$.

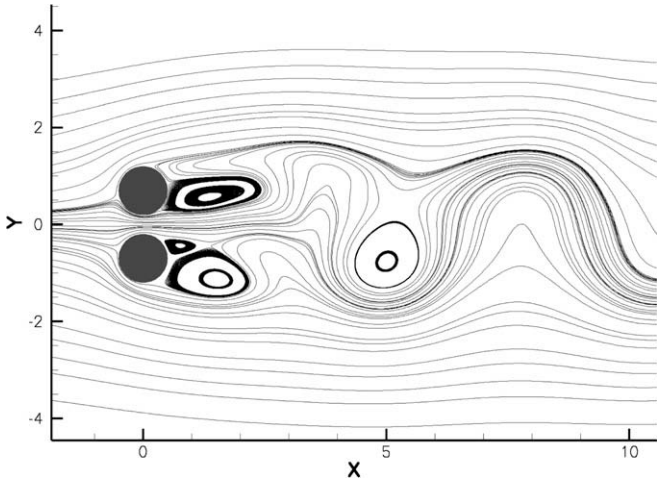

Fig. 11. Velocity streamlines for $s = 1.4$ and Re = 100.

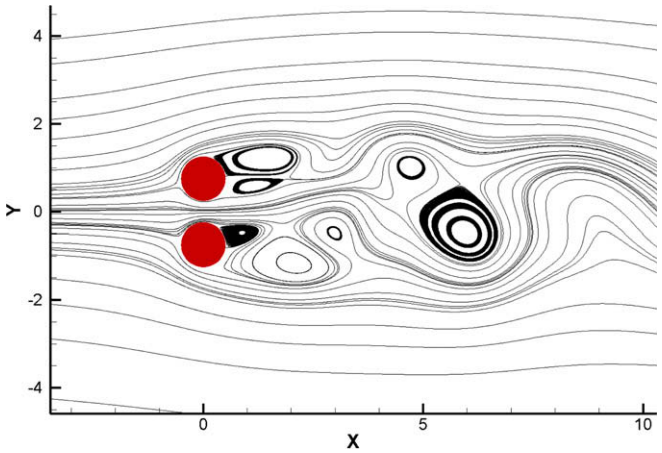

Fig. 12. Streamlines for $s = 1.5$ and Re = 100.

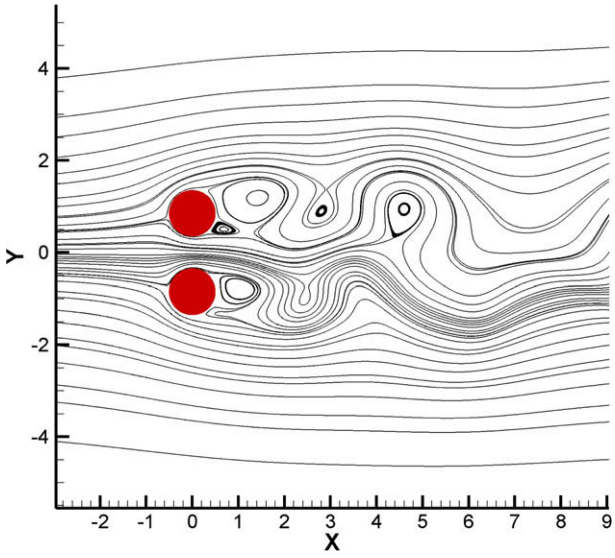

Fig. 13. Streamlines for $s = 1.7$ and Re = 100.

incompressible solver of Sharman et al. [25]. Kang [10] and Ding et al. [7] predicted higher C_l' probably due to insufficient near wall grid resolution and lower-order spatial piecewise schemes which are unable to resolve the wall curvature. The mean and rms drag coefficients are slightly higher than the ones predicted by Sharman et al. [25]. However, the presently predicted $\overline{C_d} = 1.365$ is close to 1.37 predicted by Meneghini et al. [18] and 1.356 predicted by Ding et al. [7]. The low compressibility of the present flow condition may also slightly affect mean drag coefficient but its impact is very small. Mittal and Tezduyar [20] also predicted the mean C_d around the level of 1.4 as can be seen from Fig. 7 in their paper for Mach 0.2 and Re = 100. Overall, this validation proves that the SD method predicts the correct physics for flow past a cylinder.

4. Flow past two side-by-side cylinders

4.1. Computational condition

In the following, we report simulations of flow past two side-by-side cylinders using either the third-order or 4th-order accurate SD methods. Iso-thermal wall boundary condition is employed for temperature field. Dirichlet boundary condition is applied for the left inlet boundary. The top and bottom boundaries again use symmetrical slip condition like the standard inviscid wall boundary condition Liang et al. [15]. For the right boundary, fixed pressure is specified and other values are extrapolated. If not stated otherwise, the normalized time step size $\frac{\Delta t U_\infty}{D}$ is 8×10^{-4} for all computations using the 3rd order SD method and 4×10^{-4} for all computations using the 4th order SD method.

Simulations have been carried out with two cylinders in a side-by-side arrangement for gaps/diameter in the range $1.1 \leqslant s \leqslant 4$. The point with coordinate (0, 0) is located at the middle distance between the cylinders. The free-stream Mach number is 0.1 (for $s = 1.1$, 1.4, 1.5 and 1.7) or 0.2 (for $s = 2$, 2.5, 3, 3.4 and 4) and Reynolds number is 100. As shown in Fig. 7, The inflow boundary is located at 16d in front of the cylinders. The outflow boundary is located at 32d behind the cylinders. The distance between the top and bottom boundaries is chosen as 32d. The typical computational grid for $s = 3$ case has 5106 cells (total DOFs are 45,954 and 81,696 for the 3rd-order and 4th-order SD methods respectively). Only 60 cells are used around the periphery of a cylinder surface but this number is already nearly double of the one used for the isolated cylinder testing case. The first cell near the cylinder wall is located at a distance of about 2.8% of the cylinder radius. However, considering the third-order SD method and a cubic curved boundary condition applied for the wall, the present simulation has a finer resolution than Meneghini et al. [18] who employed 128 points around the cylinder wall and the first node had a distance about 1% of cylinder radius. The present near wall grid resolution is also finer than the one used by Kang [10] with the immersed boundary method.

4.2. Results for Re = 100

In order to facilitate the discussion of flow separation points obtained from viscous skin friction coefficients, we define angular degrees in clockwise direction of a cylinder as illustrated in the Fig. 8.

At $s = 1.1$, there is no vortex generated in the gap between the two cylinders and vortices are generally shed alternately from the free-stream sides of the cylinders, thus generating a single vortex street as shown in Fig. 9. This time instant corresponds to point a, which is shown in Fig. 10. At this time instant, the lift coefficients are close to the minimum for both cylinders. For the upper cylinder, $C_l = 0.86$ and $C_d = 2.07$. The front stagnation point of the upper cylinder is at 329.5°. There is only one separation point at 133.2° and a small recirculation bubble is formed after the separation point and before the reattachment point at 141.3°. A saddle point at 243° is formed by fluid from both sides of the cylinder. The front stagnation point of the lower cylinder is at 40.8°. The fluid in the gap flows downwards and the fluid does not separate until the rear-cylinder saddle point at 248°.

As s increases, the flow regime is switched to asymmetric flow regime due to the deflected gap flow. Narrow and wide wakes are divided by the biased gap flow. As shown in Fig. 11 for $s = 1.4$,

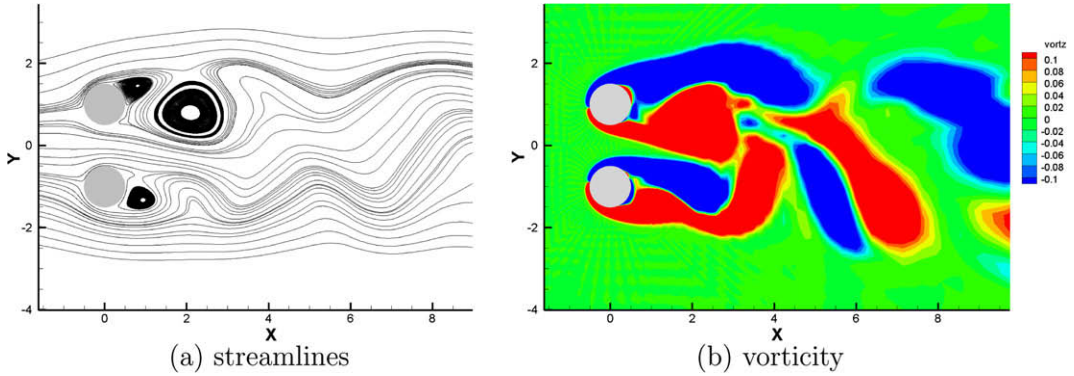

Fig. 14. Streamlines and vorticity for $s = 2$ when the gap flow upward or downward biased.

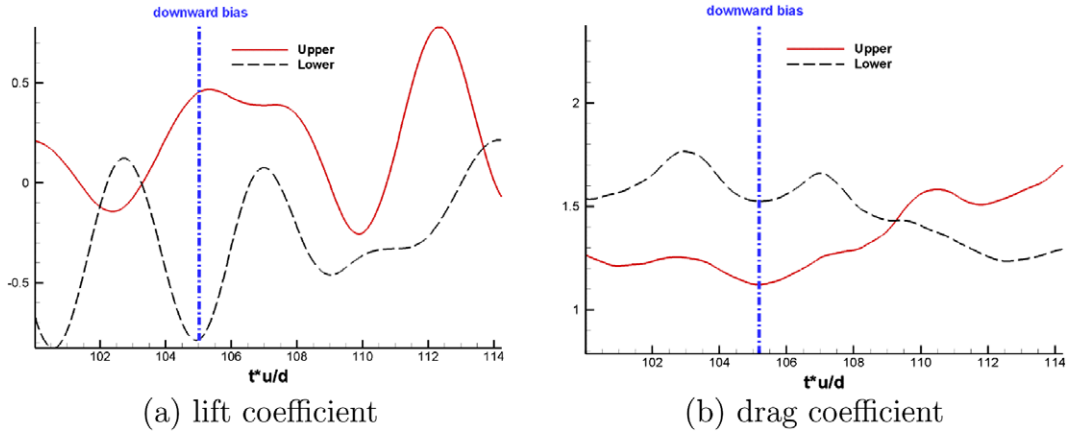

Fig. 15. Force coefficients at the time instant when the gap flow is deflected downwards for $s = 2$.

there are individual vortices shedding behind respective cylinders and their sizes are at times comparable to the cylinder diameter. At this time instant, both upper and lower cylinders have two separation points and only one reattachment point. The front stagnation point of the upper cylinder is at 342° which is nearly symmetrical to the front stagnation point of the lower cylinder at 18.3°. Two separation points of the upper cylinder are located at 107.4° and 232°. The recirculation zone reattaches to the back of cylinder at 164.8°. The horizontal length of the separation bubble formed at 232° is about two cylinder diameters. There is no noticeable recirculation bubble near the cylinder which is associated with the separation point at 107.4°. However, the separation point contributes to a recirculation bubble at $x = 5d$, which again has the size comparable to cylinder diameter. For the lower cylinder, the gap region fluid flow separates at 107.2° to form a small recirculation bubble as the flow reattaches at 178°. The bottom free-stream flow separates at 230.7° to form a recirculation bubble which is slightly bigger than the cylinder. The stream of fluid recirculates backward and joins the top side fluid flow and finally reattaches at the same location of 178°.

A little increase of cylinder spacing results in a reasonable change of wake pattern. We choose a time instant for $s = 1.5$, at which the bottom cylinder has a quite similar wake pattern as the one for $s = 1.4$. However, as shown in Fig. 12, the vortex street of the top cylinder travels in a quite different path from the one for $s = 1.4$. The stagnation point of the upper cylinder is located at 343.5°. Both cylinders have two separation points and two counter-recirculating bubble zones which are produced by the two separation points and a recirculation point. The upper

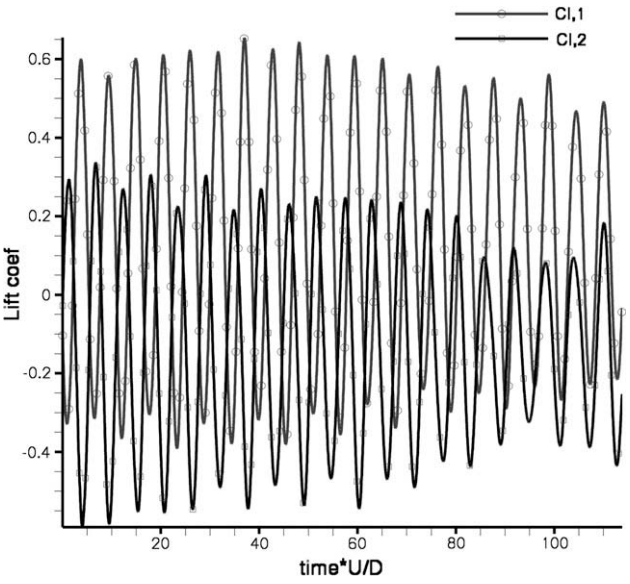

Fig. 17. Transition from anti-phase regime to in-phase regime for flow past two cylinders $s = 3$ and Re = 100.

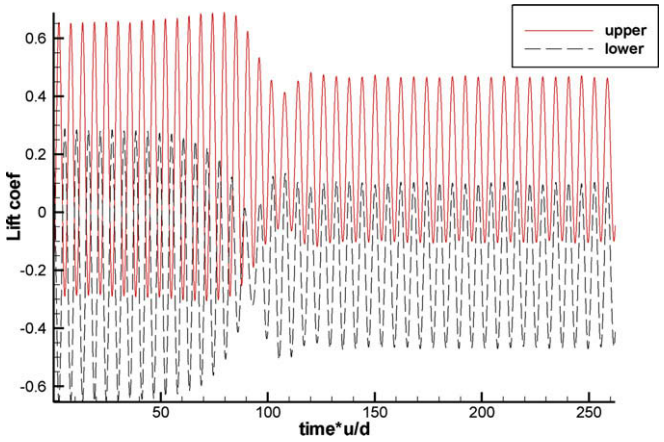

Fig. 16. Transition from anti-phase regime to in-phase regime for flow past two cylinders $s = 2.5$ and Re = 100.

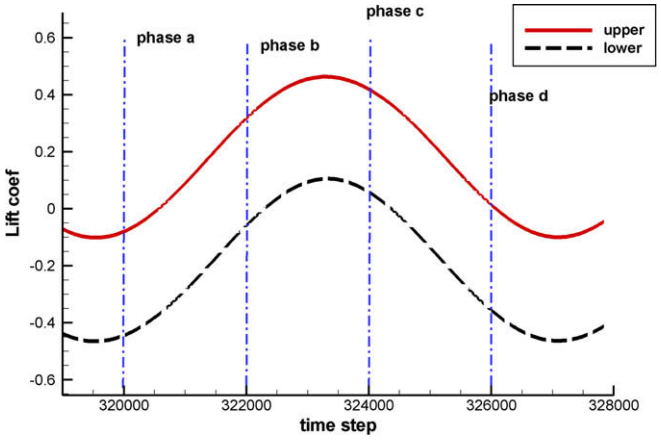

Fig. 18. Definition of four-phase snapshots for an in-phase vortex shedding flow period of flow past two cylinders with $s = 2.5$ and Re = 100.

cylinder top separation point is located at 108° and bottom separation point is located at 230.7°. The recirculation bubbles of the upper cylinder reattach at 171.9° which is smaller than its counterpart when $s = 1.4$. The gap flow contributes to a clockwise recirculation zone at $x = 4.5d$ and counter-clockwise recirculation zone at $x = 6d$.

The gap flow is deflected downwards at the time instant shown in Fig. 13 for $s = 1.7$. The upper cylinder has a front stagnation point

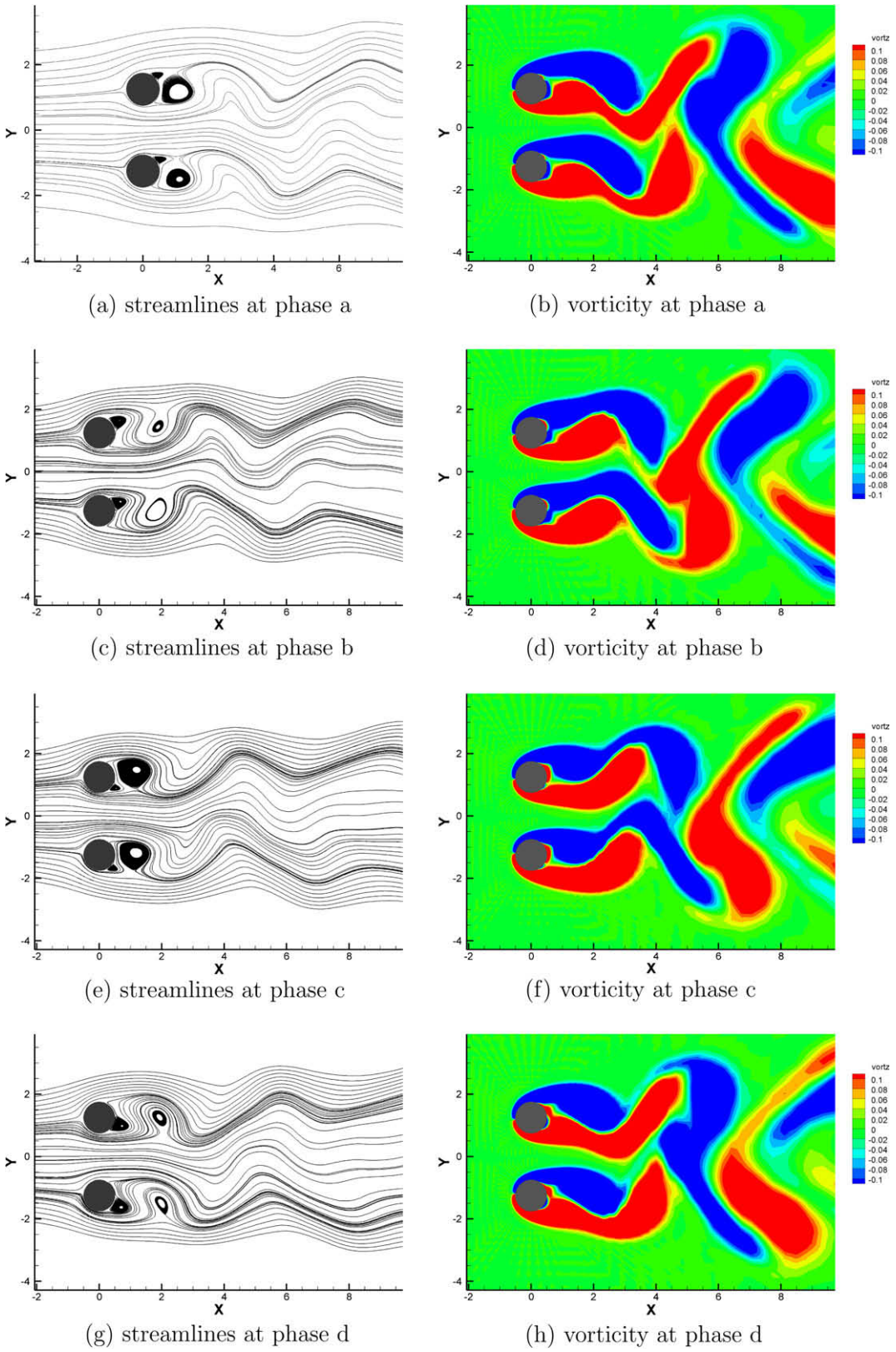

Fig. 19. Streamlines and vorticity for $s = 2.5$.

at 346.8° from freestream flow. Separation points are located at 234.8° and 109°. The reattachment point is at 193.7°. For the lower cylinder, the front stagnation point is located at 15.2°. The freestream flow and gap flow separates at 250.3° and 129.8° respectively. Similar to the upper cylinder, the reattachment point of the lower cylinder is again greater than 180° and is located at 211.6°. However, as a result of the gap flow deflection, the lift coefficients for upper and lower cylinders have different signs with $C_l^{upper} = 0.39226$ and $C_l^{lower} = -0.17664$ respectively. The instantaneous drag coefficients are $C_d^{upper} = 1.44921$ and $C_d^{lower} = 1.56845$ for the upper and lower cylinders respectively.

When $s = 2$, it is known that the near wake of the cylinder pair is asymmetric and the gap flow also becomes biased [3]. Fig. 14a and b shows the downward biased gap flow streamline and vorticity field respectively. The flow pattern has similarity with the ones at s = 1.4, 1.5 and 1.7. At the time instant shown for Fig. 14 when the gap flow is deflected downwards, the lower cylinder has a bigger C_d and higher shedding frequency than the upper one since the lower cylinder is relatively in suction pressure (see Fig. 15). This is in a good agreement with the experimental observation of Bearmann and Wadcock [2]. The lift coefficient shown in Fig. 15 also indicates that the higher-drag cylinder has a higher shedding frequency. Two Strouhal numbers 0.175 and 0.225 are identified through Fourier transformation. The former one is close to the one predicted by Kang [10].

Figs. 16 and 17 demonstrate the transition of vortex shedding wake pattern from symmetric anti-phase regime to anti-symmetric in-phase regime at Reynolds number 100. The cylinder spacings are s = 2.5 and s = 3 respectively. Initially, the lift coefficients for two cylinders are in antiphase mode (of 180° phase difference). In an interval of around 16 vortex shedding periods, the difference gradually reduces and converges to in-phase mode (0° phase difference). Chang and Song [3] also observed from the time history of C_l that the vortex drifts with time from the anti-phase regime to in-phase regime. During the in-phase regime, the top separation point angle of the upper cylinder θ^1_{upper} is located at an identical degree to the one of the lower cylinder θ^1_{lower}.

Fig. 18 defines four-phase snapshots for an in-phase vortex shedding period for s = 2.5 and Re = 100 case using the time history of C_l. Fig. 19 visualizes the streamlines and vorticity contour for four different phases defined in Fig. 18. At phase a, the fluid which flows from the bottom side of the cylinders forms a pair of vortices with identical size as seen in the streamlines. At this time instant, both cylinders are having negative lift force. Further downstream

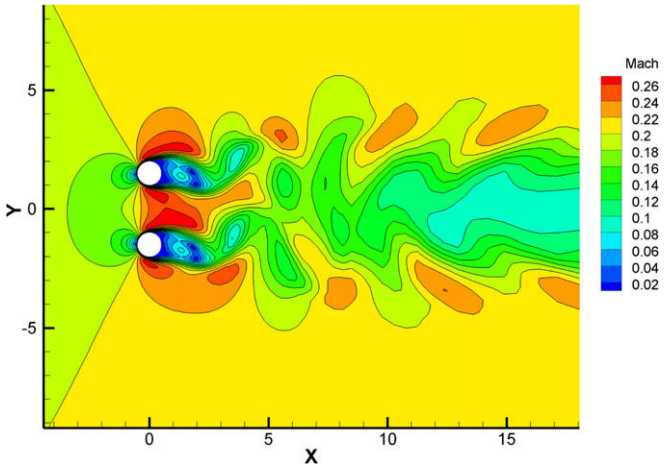

Fig. 20. Instantaneous Mach number contour computed for flow past two cylinders s = 3 and Re = 100.

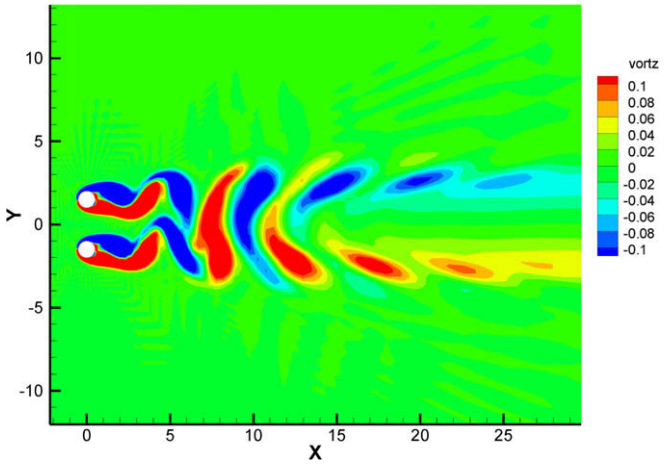

Fig. 21. Instantaneous vorticity contour computed for flow past two cylinders s = 3 and Re = 100.

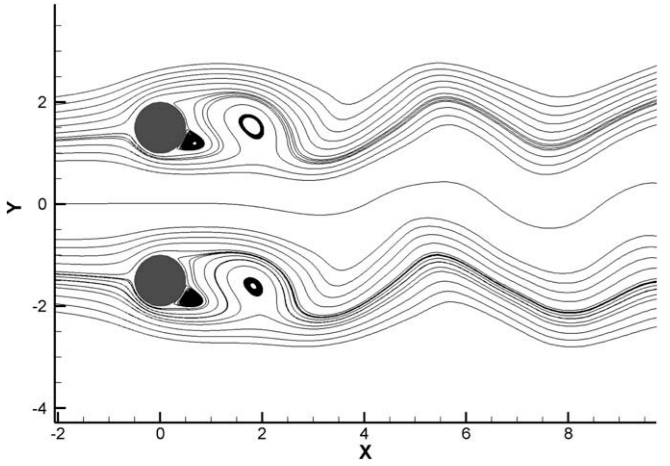

Fig. 22. Instantaneous streamlines computed for flow past two cylinders s = 3 and Re = 100.

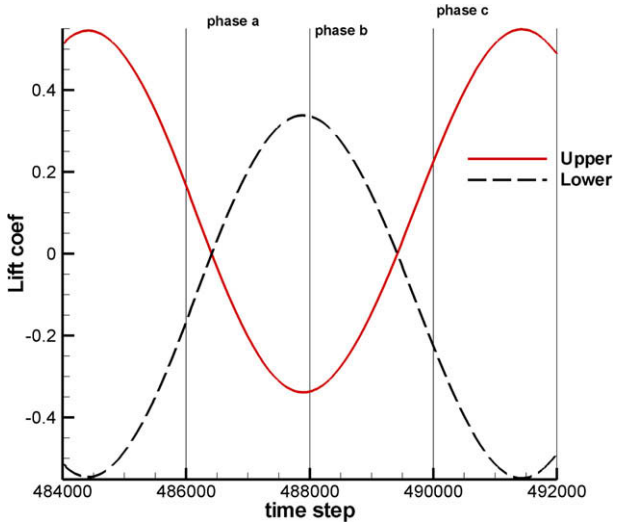

Fig. 23. Definition of three-phase snapshots for an anti-phase vortex shedding flow period of flow past two cylinders with s = 3.4 and Re = 100.

when $x \geqslant 5$, vortices from upper and bottom merge across the centerline to form an elongated single vortex and simultaneously two vortex streets merge to a single wide vortex street. Similarly, at phase b, the fluid which flows from the top side of cylinders start

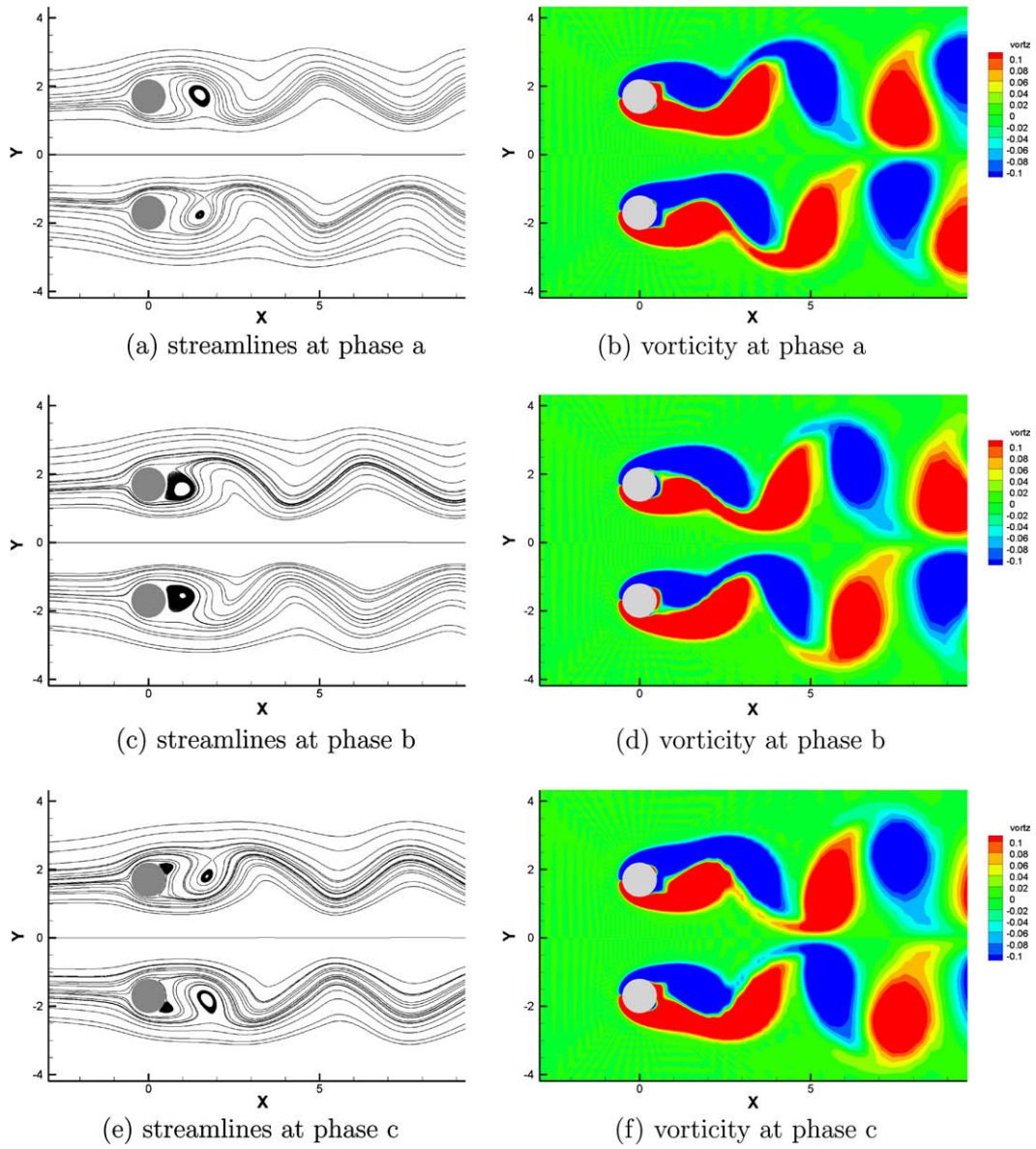

Fig. 24. Streamlines and vorticity for $s = 3.4$.

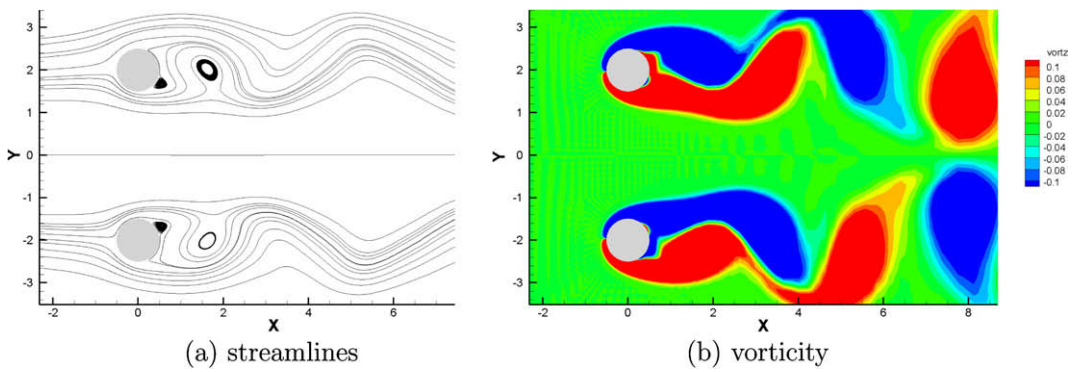

Fig. 25. Streamlines and vorticity for $s = 4$.

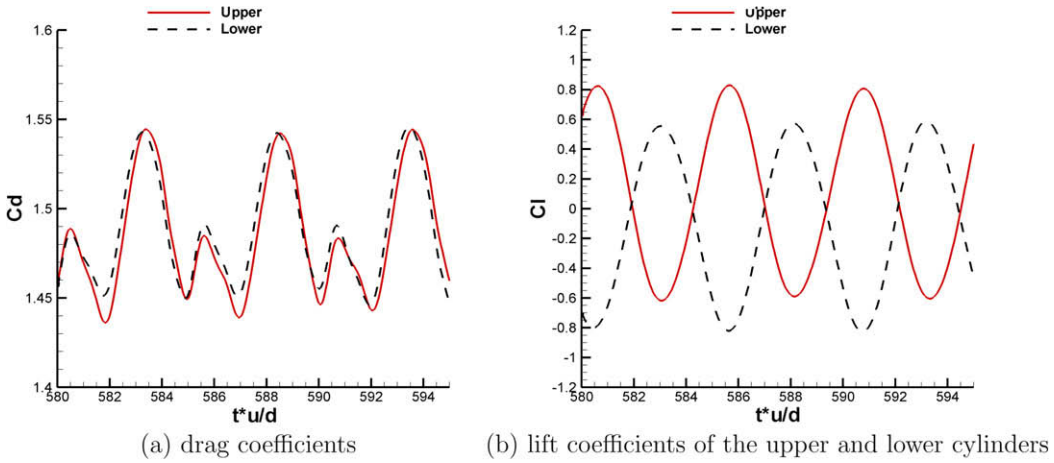

(a) drag coefficients (b) lift coefficients of the upper and lower cylinders

Fig. 26. Force coefficients for the case of Re = 150 and $s = 3$.

to form vortices in proximity of the top corners of the cylinder pair. These vortices grow in size and result in top-side low pressure regions leading to two positive lift force coefficients for two cylinders at the time instant of phase c. As the two big vortices convect away, C_l decreases as shown for phase d. A dramatic feature of these phases is that upper and lower cylinders are having nearly identical flow structures in their near wakes at any time instant. At this spacing, vortex shedding patterns from two cylinders are strongly synchronized to form an exactly anti-symmetrical wake pattern.

Fig. 20 shows the Mach number distribution of the asymmetric in-phase vortex shedding at Re = 100 and $s = 3$. The high-Mach region ($0 \leqslant x \leqslant 4d$) in the gap starts to fluctuate in the transverse direction. In the further downstream along the center line, there is a continuous low-Mach number distribution. Fig. 21 shows the vorticity distribution of the asymmetric in-phase vortex shedding at Re = 100 and $s = 3$. In between $x = 6d$ and $x = 13d$, there is no longer symmetric pairs of opposite-sign vortices as they are merged into an elongated single vortices in the transverse direction. Further downstream ($x \leqslant 13$), the central line region is associated with a low-magnitude vorticity. Fig. 22 presents the streamlines of the antisymmetric in-phase vortex shedding at Re = 100 and $s = 3$. The vortex rows merge through a combination of vortices of the same sign with a fluctuating middle stream line, as Williamson [31] has shown using flow visualization methods. In the downstream region, the merged vortex rows form a single vortex street as already observed in the vorticity contour plot in Fig. 21.

Wake patterns of the upper and lower cylinders have a phase difference of 180° for the case of $s = 3.4$ and Re = 100. It is evident from the lift coefficients as shown in the Fig. 23. Phase b corresponds to a time instant at which the C_l is minimum and maximum for the lower and upper cylinders respectively. The summation of the top separation point angle of the upper cylinder θ^1_{upper} and the bottom separation point angle of the lower cylinder θ^3_{lower} is 360°, i.e. $\theta^1_{upper} + \theta^3_{lower} = 360°$. Fig. 24 visualizes the streamlines and vorticity contour for three different phases defined in Fig. 23. The anti-phase vortex shedding pattern is very stable and maintains a long time period as the upper cylinder wake does not seem to interact with the one of the lower cylinder.

Despite the difference predicted for the transitional regime at $s = 3$ by different numerical methods in published literatures, previous numerical studies agree that $s = 4$ has a symmetric anti-phase synchronized vortex shedding pattern [3,18,10,7]. The SD method also predicts a very stable symmetric vortex shedding as shown in Fig. 25. The wake patterns of streamlines and vorticity are very similar to those obtained for $s = 3.4$.

4.3. Reynolds number dependence

Having predicted the anti-symmetric flow pattern for Re = 100 at $s = 3$ and having noted that Zhou et al. [36] observed symmetric flow pattern for Re = 150, we performed two-dimensional simulations of the same flow ($s = 3$) at Reynolds numbers 150 and 200. The synchronization for vortex shedding can be observed from the time history of drag coefficients shown in Fig. 26a. This is in a good agreement with the symmetric wake pattern visualized by Zhou et al. [36]. The upper and lower cylinders have nearly the same C_d in both phase and magnitude. The lift coefficients for the upper and lower cylinders are 180° out of phase as shown in Fig. 26b. Fig. 27 shows the streamlines at the time instant, at which the lift coefficient of the upper cylinder attains its maximum and the one of the lower cylinder reaches the minimum.

Fig. 28 shows the difference of mean C_l, C_d and rms C_l, C_d as well as the Strouhal number of the upper cylinder for Reynolds numbers 100, 150 and 200. As the Reynolds number increases, the mean C_l decreases but all other values increase. It is also noted that the rms values of force coefficients are generally smaller than those predicted by other simulations (using low-order accurate schemes). The Strouhal number distribution has a fair agreement with other numerical studies. It has big jump between Re 100

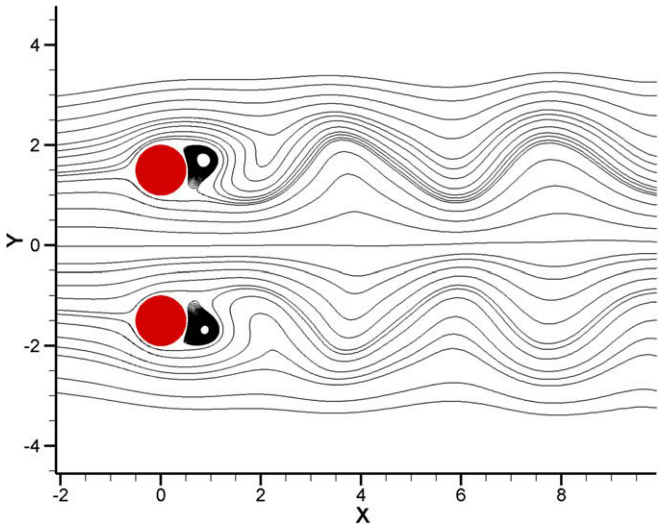

Fig. 27. Instantaneous streamlines for flow past side-by-side cylinders at Re = 150 and $s = 3$.

and 150 and then increases slowly between 150 and 200. These values are comparable to the experimental values for single cylinder presented by Williamson [32,33] as shown in Fig. 28e. The Strouhal numbers for the cylinder pair are only slightly higher than those of the isolated cylinders at Re 100 and 200 respectively. The predicted Strouhal number lies just in between the ones predicted by Meneghini et al. [18] and Ding et al. [7] for Re 200.

Fig. 29 shows the Mach number distribution of the symmetric anti-phase vortex shedding at Re = 200 and $s = 3$. Along the center line, high and low values of Mach number are alternatively distributed. In particular, these high-Mach zones are surrounded completely in all directions by low-Mach regions. They do not fluctuate in the transverse direction and they are indeed different from the fluctuating ones in Fig. 20. Fig. 30 shows the vorticity distribution of the symmetric anti-phase vortex shedding at Re = 200 and $s = 3$. The center line divides more than 10 pairs of symmetric opposite-sign vortices in the region of $0 \leqslant x \leqslant 20d$. In the near wake ($2d \leqslant x \leqslant 15d$), adjacent vortices aligned in a straight horizontal line and neighboring vortices have opposite signs. Further downstream ($x \geqslant 15d$), at the same streamwise location, there

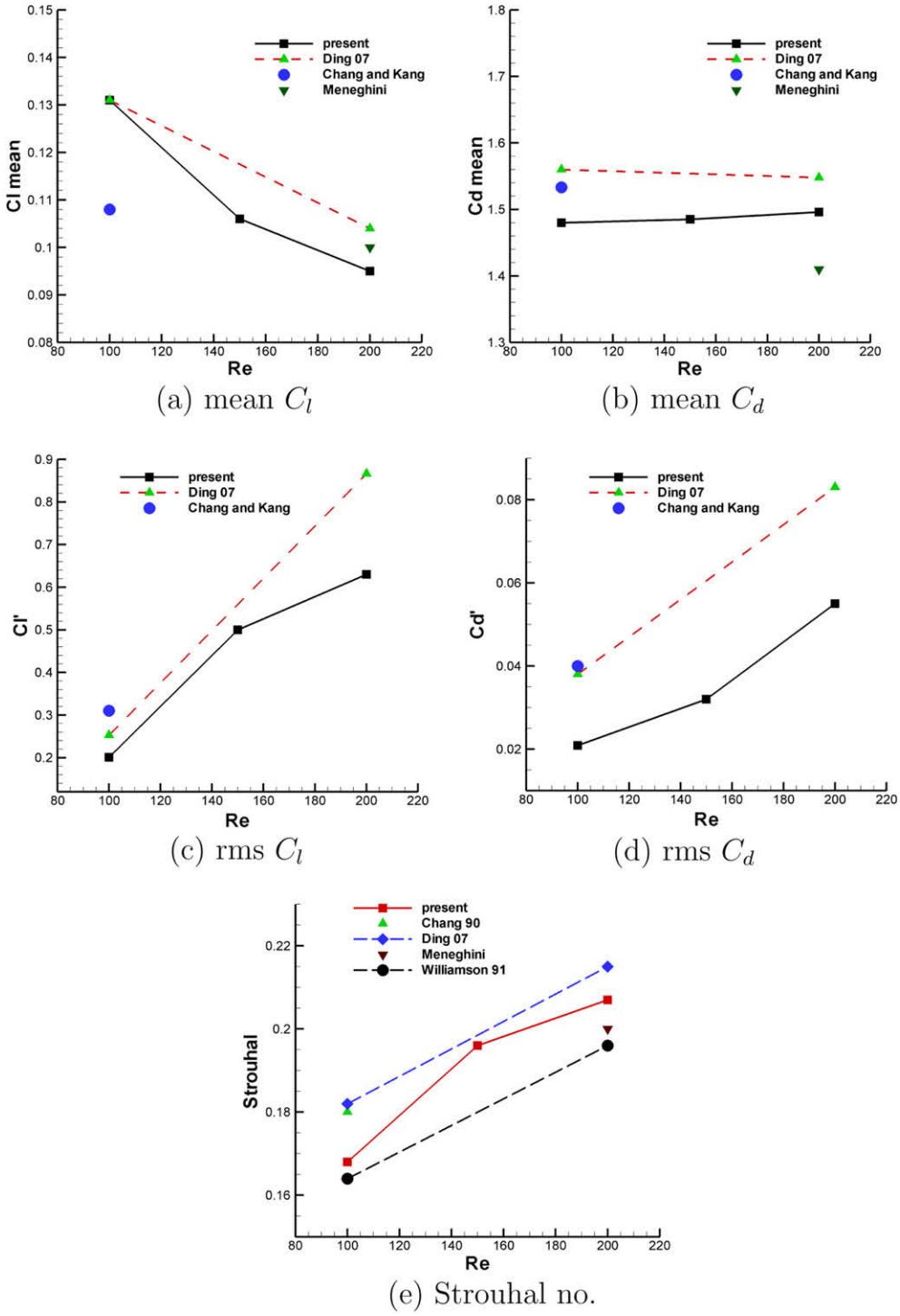

Fig. 28. Reynolds number dependence for force statistics and Strouhal number at $s = 3$.

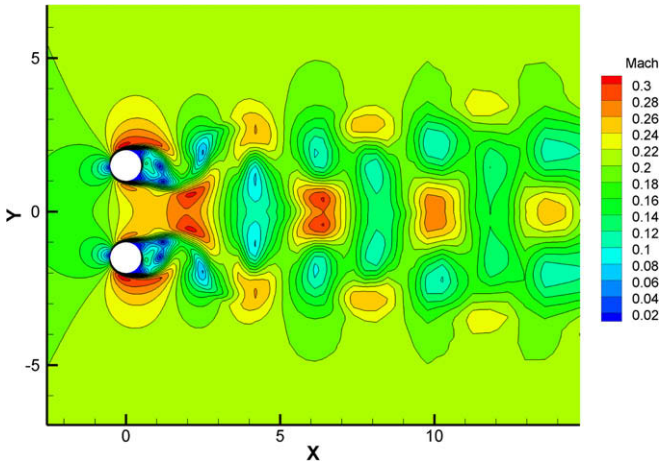

Fig. 29. Instantaneous Mach number contour computed for flow past two cylinders $s = 3$ and Re = 200.

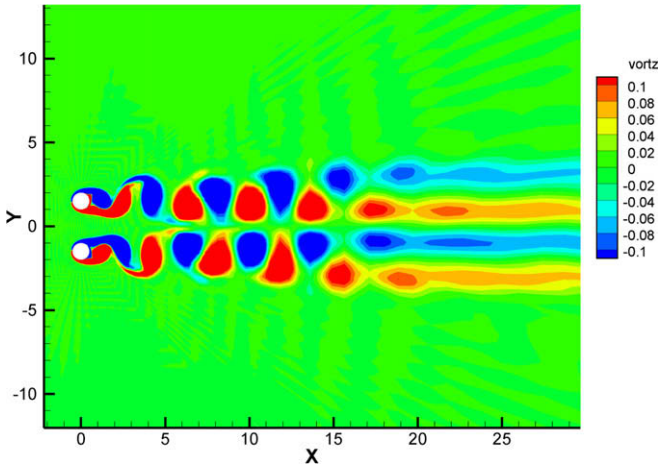

Fig. 30. Instantaneous vorticity contour computed for flow past two cylinders $s = 3$ and Re = 200.

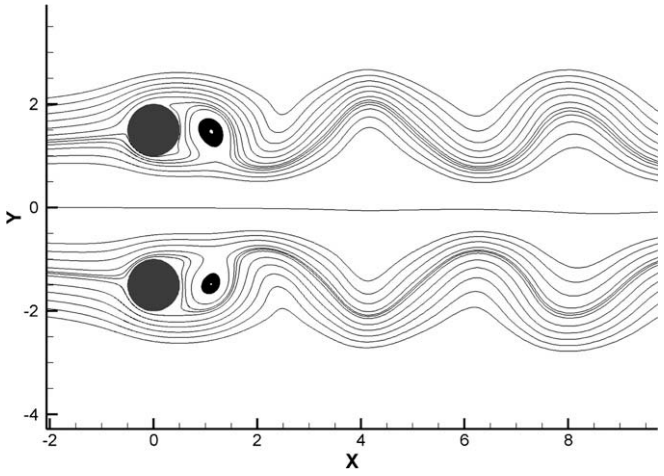

Fig. 31. Instantaneous streamlines computed for flow past two cylinders $s = 3$ and Re = 200.

are two pairs of opposite-sign vortices in the transverse direction. In contrast to Fig. 22, Fig. 31 presents the streamlines of the symmetric anti-phase vortex shedding at Re = 200 and $s = 3$. The vortex rows do not merge across the middle straight line.

5. Conclusion

We have developed a high-order unstructured solver with the spectral difference method for inviscid and viscous flows. We verified that our presently developed two-dimensional solver on quadrilateral grids could achieve the desired numerical order on both inviscid and viscous flows. The SD method is then applied to simulate flow past two side-by-side cylinders. At $s = 1.1$, wake flow pattern resembles the vortex street of a single bluff body. At $s = 1.4$, 1.5, 1.7 and 2, we predicted asymmetric flow patterns for flow past the cylinder pair and the separation points of the upper and lower cylinders are not synchronized. Anti-symmetric in-phase flow patterns are predicted for arrangements with $s = 2.5$ and 3 at Reynolds number 100. The unsteady flow of the upper and lower cylinders separate at locations of the same degrees on the cylinder surfaces. On further increasing the distance between two cylinders to $s = 3.4$ and 4, the symmetric anti-phase flow patterns are observed. The separation points of the upper and the lower cylinders are symmetrical across the centerline of the gap flow. Some flow parameters such as the Strouhal number, mean and rms values of lift and drag coefficients, which quantitatively characterize the flow fields are predicted and are in good comparison with those of previous studies for $s = 3$ and Re = 100. The flow patterns of the Reynolds numbers 150 and 200 for $s = 3$ are no longer in-phase synchronized but maintain a stable symmetric anti-phase synchronized vortex shedding pattern.

Acknowledgements

The authors would like to thank the grant supports from NSF monitored by Dr Leland Jameson and AFOSR monitored by Dr Fariba Fahroo. Chunlei Liang would also like to thank Professor Z. J. Wang for discussions regarding the two-dimensional SD scheme and Andre S. Chan for discussion about the flow physics of two side-by-side cylinders.

References

[1] Bassi F, Rebay S. High-order accurate discontinuous finite element solution of the 2d Euler equations. J Comput Phys 1997;138:251–85.
[2] Bearmann PW, Wadcock AJ. The interaction between a pair of circular cylinders normal to a stream. J Fluid Mech 1973;61:499–511.
[3] Chang KS, Song CJ. Interactive vortex shedding from a pair of circular cylinders in a transverse arrangement. Int J Numer Meth Fluids 1990;11:317–29.
[4] Cockburn B, Shu C-W. TVB Runge–Kutta local projection discontinuous Galerkin finite element method for conservation laws II: general framework. Math Comput 1989;52:411–35.
[5] Cockburn B, Shu C-W. The Runge–Kutta discontinuous Galerkin method for conservation laws V: multidimensional systems. J Comput Phys 1998;141:199–224.
[6] Debonis JR, Scott JN. A large-eddy simulation of a turbulent compressible round jet. AIAA paper AIAA-2001-2254; 2001.
[7] Ding H, Shu C, Yeo KS, Xu D. Numerical simulation of flows around two circular cylinders by mesh-free least square-based finite difference methods. Int J Numer Meth Fluids 2007;53:305–32.
[8] Harten A, Hyman JM. Self-adjusting grid methods for one-dimensional hyperbolic conservation laws. J Comput Phys 1983;50:235–69.
[9] Huang Z, Olson JA, Kerekes RJ, Green SI. Numerical simulation of the flow around rows of cylinders. Comput Fluids 2006;35:485–91.
[10] Kang S. Characteristics of flow over two circular cylinders in a side-by-side arrangement at low Reynolds numbers. Phys Fluids 2003;15:2486–98.
[11] Lee K, Yang KS, Yoon DH. Flow-induced forces on two circular cylinders in proximity. Comput Fluids 2009;38:111–20.
[12] Li T, Deen NG, Kuipers JAM. Numerical investigation of hydrodynamics and mass transfer for in-line fiber arrays in laminar cross-flow at low Reynolds numbers. Chem Eng Sci 2005;60:1837–47.
[13] Liang C, Kannan R, Wang ZJ. A p-multigrid spectral difference method with explicit and implicit smoothers on unstructured triangular grids. Comput Fluids 2009;38:254–65.

[14] Liang C, Papadakis G. Large Eddy Simulation of flow over a staggered tube bundle at subcritical Reynolds number. J Fluids Struct 2007;23:1215–30.
[15] Liang C, Premasuthan S, Jameson A, Wang ZJ. Large eddy simulation of compressible turbulent channel flow with spectral difference method. In: 47th AIAA aerospace sciences meeting including the new horizons forum and aerospace exposition, AIAA Paper 2009-402. Florida: Orlando; 2009.
[16] Liu Y, Vinokur M, Wang ZJ. Spectral difference method for unstructured grids I: basic formulation. J Comput Phys 2006;216:780–801.
[17] Liu Y, Vinokur M, Wang ZJ. Spectral (finite) volume method for conservation laws on unstructured grids V: extension to three-dimensional systems. J Comput Phys 2006;212:454–72.
[18] Meneghini JR, Saltara F, Siqueira CLR, Ferrari JA. Numerical simulation of flow interference between two circular cylinders in tandem and side-by-side arrangements. J Fluids Struct 2001;15:327–50.
[19] Michalak C, Ollivier-Gooch C. Unstructured high-order accurate finite-volume solutions of the Navier-Stokes equations. AIAA paper, AIAA-2009-954. Florida: Orlando; 2009.
[20] Mittal S, Tezduyar T. A unified finite element formulation for compressible and incompressible flows using augmented conservation variables. Comput Meth Appl Mech Eng 1998;161:229–43.
[21] Mohammad AH, Wang ZJ, Liang C. Large Eddy Simulation of flow over a cylinder using high-order spectral difference method. AIAA paper AIAA-2008-7184; 2008.
[22] Ragab SA, El-Okda YM. Applications of a fifth-order non-centered compact scheme for Large Eddy Simulation. AIAA paper AIAA-2005-1267; 2005.
[23] Roe PL. Approximate riemann solvers, parameter vectors and difference schemes. J Comput Phys 1981;43:357–72.
[24] Rusanov VV. Calculation of interaction of non-steady shock waves with obstacles. J Comput Math Phys USSR 1961;1:261–79.
[25] Sharman B, Lien FS, Davidson L, Norberg C. Numerical predictions of low Reynolds number flows over two tandem circular cylinders. Int J Numer Meth Fluids 2005;47:423–47.
[26] Spiteri RJ, Ruuth SJ. A new class of optimal high-order strong-stability-preserving time discretization methods. SIAM J Numer Anal 2002;40:469–91.
[27] Sun Y, Wang ZJ, Liu Y. High-order multidomain spectral difference method for the Navier–Stokes equations on unstructured hexahedral grids. Commun Comput Phys 2007;2:310–33.
[28] Wang Z, Liu Y, May G, Jameson A. Spectral difference method for unstructured grids II: extension to the Euler equations. J Sci Comput 2007;32:45–71.
[29] Wang ZJ. Spectral (finite) volume method for conservation laws on unstructured grids: I Basic formulation. J Comput Phys 2002;178:210–51.
[30] Wang ZJ, Liu Y. Extension of the spectral volume method to high-order boundary representation. J Comput Phys 2006;211:154–78.
[31] Williamson CHK. Evolution of a single wake behind a pair of bluff bodies. J Fluid Mech 1985;159:1–18.
[32] Williamson CHK. Oblique and parallel modes of vortex shedding in the wake of a circular cylinder at low Reynolds numbers. J Fluid Mech 1989;206:579–627.
[33] Williamson CHK. 2D and 3D aspects of the wake of a cylinder, and their relation to wake computations. Lect Appl Math 1991;28:719–51.
[34] Zdravkovich MM. Review of flow interference between two circular cylinders in various arrangements. ASME J Fluids Eng 1977;99:618–33.
[35] Zdravkovich MM. The effects of interference between circular cylinders in cross flow. J Fluids Struct 1987;1:239–61.
[36] Zhou Y, Wang ZJ, So RMC, Xu SJ, Jin W. Free vibrations of two side-by-side cylinders in a cross flow. J Fluid Mech 2001;443:197–229.